



Morphology effect of metal-insulator-metal nanopatch antennas in strong coupling with monolayer WSe₂

ZHIWEI HU,^{1,†} SI KAN,^{1,†} XIAOBO HAN,^{1,3}  HUATIAN HU,^{1,4} 
CHAO GUAN,² AND KAI WANG² 

¹Hubei Key Laboratory of Optical Information and Pattern Recognition, Wuhan Institute of Technology, Wuhan 430205, China

²Wuhan National Laboratory for Optoelectronics and School of Physics, Huazhong University of Science and Technology, Wuhan 430074, China

³hanxiaobo@wit.edu.cn

⁴huatian.hu@iit.it

[†]The authors contributed equally to this work.

Abstract: Serving as cavity quantum electrodynamic testbeds at the nanoscale, the past decade has seen a prosperous rise in strong coupling between metallic nanostructures and semiconductor excitons. Within the iteration of the delicate plasmonic nanostructures, metal-insulator-metal (e.g., various nanoparticles-on-mirror) planar structures with highly confined fields and decent quality factors, come to prominence. Excitons in transition metal dichalcogenides (TMDCs) emerge as a favored choice of quantum emitters due to their room-temperature performance and potential integration into optoelectronic devices. In this paper, strong coupling with a Rabi splitting of 137 meV was achieved by coupling radial breathing mode from a nanoplate-on-mirror planar nanoantenna with neutral excitons in monolayer WSe₂. More importantly, we investigated the morphology dependence of the coupling in planar nanopatch antennas. It showed that the efforts taken to change the shapes and sizes of the nanopatch structures (e.g., hexagonal, triangular, round plates, etc.) can not effectively optimize the coupling. This is because only the excitons at the edges could contribute to the coupling strength. It is double-edged that, on the one hand, it sets a limitation for tuning the coupling strength, on the other hand, it prevents involving more excitons which may degrade the plexcitonic nonlinearity.

© 2025 Optica Publishing Group under the terms of the [Optica Open Access Publishing Agreement](#)

1. Introduction

When the energy exchange between two subsystems is faster than their dissipative dynamics, the interaction steps into a so-called strong coupling regime [1–6]. In this regime, the quasiparticle behavior of plexcitons (plasmon-exciton hybrids) could help pass the strong nonlinearity from the excitons to the photons which have purely linear performance [7,8]. In the past decades, researchers have spared no effort in establishing plexcitonic systems with great Rabi frequencies [9–24], while simultaneously keeping fewer excitons involved [25–29]. In principle, only fewer-excitons participated strong coupling can truly reflect quantum mechanical effects. The strong light-matter interaction in solid-state systems which have potential applications in quantum computing [30,31], low-threshold lasers [32–34], quantum information storage and processing [35,36].

Among different structures, the planar nanopatch antennas have aroused great interest due to the well-defined bottom-up for top-down fabrication, ultrasmall mode volumes, high quality factors, etc [9–14]. With microscopic metal-insulator-metal features formed by the nanogaps between the bottom of the nanoparticles (NPs, nanospheres, nanocubes, plates etc.) and the metal substrate, the antenna could easily concentrate the field into an extremely confined regime

in the spacer [37]. With the lowest [12–15] or higher [10,17,26] order modes of the antenna, a lot of efforts have been taken in order to increase the Rabi splitting by optimizing the shapes, and sizes of the antenna. Yet, the optimization remains limited, there are still no outstanding improvements being observed.

This paper aims to study and compare the coupling performance of the general nanopatch antenna with excitons from monolayer TMDCs. The higher order modes were applied in order to get a simultaneously small mode volume and linewidth, which may benefit the coupling. As for proof-of-principle demonstration, the radial breathing modes (RBM) of the hexagonal nanoplate (flat-plate particle) and monolayer WSe₂ excitons were coupled, and a Rabi splitting of 137 meV was achieved. Compared with the previous strong coupling systems between single particle and monolayer WSe₂ [19–22], we have achieved both large splitting energy (> 100 meV) and large criteria parameter $2g/(\Gamma_p + \Gamma_0) = 0.7$, satisfying the stricter strong coupling criterion. The origin and evolution of this breathing mode were clearly revealed in the language of plasmon hybridization, i.e., bonding octuple-octuple modes. Its evolution with the change the morphology shows that the breathing modes are robust and independent of the shapes. It would further degenerate with the l_{01} antenna modes when the hexagonal plate is reshaped into a round disk. These results in general give a landscape of general nanopatch-like configurations, and the modes researchers usually investigate only have non-zero in-plane field around the edges, which won't help much with enhancing the Rabi splitting. Instead, the rounding curvature at the corners plays much significant roles in both boosting Rabi splitting and shrinking down the number of involved excitons.

2. Radial breathing mode of the planar nanopatch antenna

As a representative of the nanopatch antenna, we composed a synthesized hexagonal Au nanoplate with an Ag film (HNPM) spaced by an Al₂O₃ thin layer (Figs. 1(a),(b)). The flat bottom facet of the nanoplate and the metallic substrate formed a well-defined metal-insulator-metal configuration that can support a series of confined nanocavity modes. Instead of using the fundamental magnetic resonance of the nanopatch antenna, we take advantage of the higher-order plasmon called radial breathing mode [38–40]. The scattering of the HNPM was simulated according to the parameters given by the scanning electron microscope image (Fig. 1(b)): the length of the nanoplate defined by the distance between parallel edges equals 170 nm, height of the nanoplate is 40 nm. The nanoplate was covered by CTAB with a thickness of 2-4 nm. See S1 in Supplement 1 for more simulation details.

Figure 1(c) presents three prominent nanocavity resonances of the HNPM at 1.8, 1.6 and 1.1 eV. The charge distributions of each resonance in the inset have one, two, and three pairs of nodes in the mode profiles, manifesting a dipole-, quadrupole-, and octopole-like resonance, respectively. To investigate the origin of the RBM, we conducted detailed simulations of a GHN on an Ag film with various gap thickness in Fig. S2a. To name each resonance based on a language of plasmon hybridization, in Fig. S2b we also provide detailed simulations of the simplified structures as nanoparticle dimers. In Fig. 1(c), we show the scattering spectra of GHNs on an Ag film with a 9 nm thick spacer layer (Al₂O₃). The magnetic mode (mode I, near 1100 nm, represented by green triangles) and RBM (mode III, near 700 nm, represented by red triangles) are bright, while the quadrupole mode (mode II, near 750 nm, represented by blue triangles) is dark. Figure 1(d) displays the in-plane electric field distribution of the RBM. The in-plane electric field enhancement of the RBM is much stronger than that of the ordinary quadrupole mode. And if we compare these three eigenmodes, we can easily see that the in-plane component of the electric field only situates at the edges of the NPs. It could be easily understood as analogous to the electric field of a parallel plate capacitor. Therefore, only the excitons which are near the edge of the nanocavities can be involved in the coupling process.

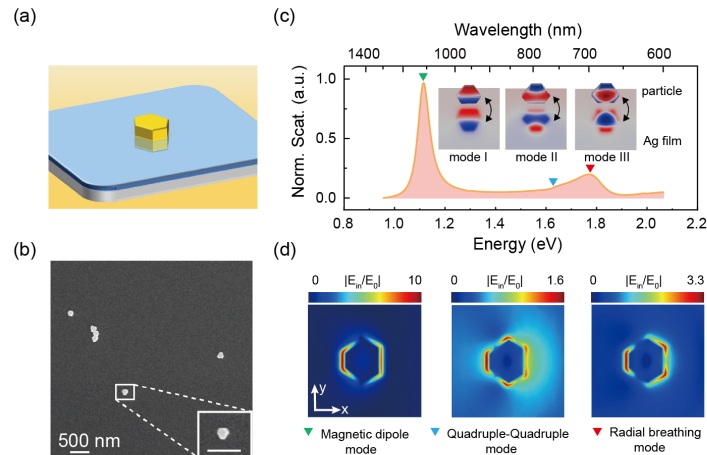


Fig. 1. The modes analysis of a single nanoplate-on-mirror cavity. (a) Schematic of a single Au hexagonal nanoplate (GHN) on an Ag film. (b) A typical SEM image of single nanoplates on the Ag film. (c) Simulated scattering spectra of the Au nanoplate-on-film with a 9-nm thick Al_2O_3 . Insets are the charge distribution of the magnetic dipole mode (mode I, green marker), quadrupole mode (mode II, blue marker), and radial breathing mode (RBM) (mode III, red marker). (d) In-plane electric field distribution of the three modes.

3. Strong coupling between HNPoM and monolayer WSe_2 : experiments

As a cavity higher-order mode, the RBM resonance can well match the energy of the excitons in the visible range, such as neutral exciton from monolayer WSe_2 . The hybrid system consists of single GHNs on an Ag film separated by monolayer WSe_2 and Al_2O_3 , as shown in Fig. 2(a). In the experiment, the hybrid nanocavities were fabricated using a bottom-up nanoassembly. First, the Ti/Ag film was deposited by electron-beam evaporation, then the spacer layer of Al_2O_3 was coated by atomic layer deposition (ALD). Monolayer WSe_2 fabricated by chemical vapor deposition (CVD) was then transferred with the help of PDMS. The GHNs capped with the residual CTAB were then sparsely deposited onto the monolayer WSe_2 by drop-casting. The size of GHNs ranges from 130 nm to 180 nm with a thickness of 40 nm. In Fig. 2(a), a scanning electron microscopy (SEM) image of the hybrid nanocavity further confirms its individual dispersion and polygonal morphology. Note that single GHNs are generally not standard hexagons, but shapes between regular hexagons and regular triangles. Thereby, the simulation model is based on non-standard hexagons.

By adjusting the thickness of the Al_2O_3 layer to 9 nm, the resonance energy of the RBM matches the exciton energy well. A typical dark-field scattering spectrum and the photoluminescence (PL) spectrum of monolayer WSe_2 with a peak at 710 nm are plotted in Fig. 2(c). Dark-field scattering spectra were measured at the single particle level on an upright optical microscope (Olympus, BX53) equipped with a spectrometer (Andor, 303i) as shown in Fig. S3 [13]. Several nanoplates of different sizes were measured, and the scattering spectra are displayed in Fig. 2(d). It can be seen that a fixed dip appeared at the exciton energy of monolayer WSe_2 . The RBM progressively varied from high to low energies, crossing the exciton transition energy at 1.75 eV. The mode splitting occurs in all scattering spectra. Additionally, the scattering spectra of the hybrid nanocavities are simulated to understand the coupling mechanism. In the simulation, the permittivity of the WSe_2 is anisotropic with the in-plane components modeled as a Lorentz oscillator. By tuning the size of nanoplate, similar scattering spectra can be obtained as shown in Fig. 2(d). This variation trend is generally in agreement with that observed in our experiments.

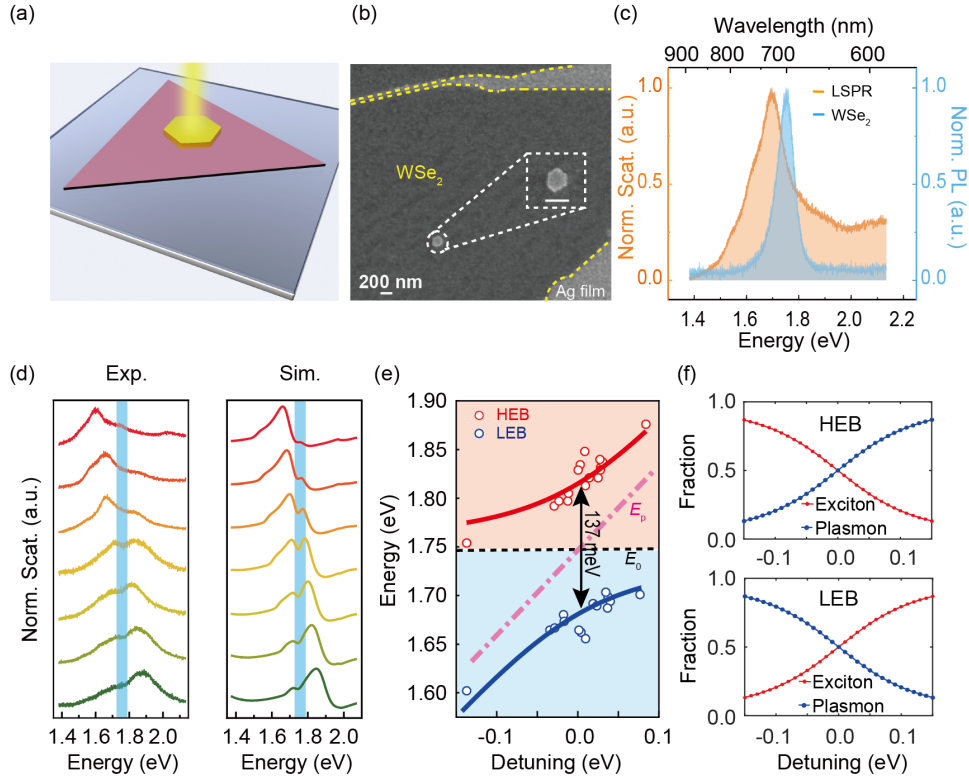


Fig. 2. Strong coupling between HNPoM and monolayer WSe₂. (a) Schematic of the hybrid nanocavity with monolayer WSe₂ integrated into the gap region of the HNPoM structure. The pink triangle represents the monolayer WSe₂. (b) SEM image of the hybrid nanocavity. The darker grey areas correspond to WSe₂, and the lighter ones to Ag film. Inset shows the enlarged hexagonal Au nanoplate. (c) Dark-field scattering spectra of HNPoM, and the PL spectra of monolayer WSe₂. (d) Measured and simulated scattering spectra of the hybrid nanocavities acquired from different nanoplates. The light blue areas denote the exciton energy position. (e) Dispersion curves of hybrid nanocavities as a function of detuning. Blue and red dots denote the spectral peaks extracted from experimental scattering spectra. The solid lines represent the fitting results obtained from the coupled oscillator model. (f) Hopfield coefficients for the HEB and LEB.

Further, we extract the energy peaks from the measured scattering spectra and plot the dispersion diagram, showing the anti-crossing curve in Fig. 2(e). The mixed states can be described using the coupled oscillator model [15–19]

$$\begin{pmatrix} E_p - i\Gamma_p/2 & g \\ g & E_0 - i\Gamma_0/2 \end{pmatrix} \begin{pmatrix} \alpha \\ \beta \end{pmatrix} = E_{\pm} \begin{pmatrix} \alpha \\ \beta \end{pmatrix} \quad (1)$$

where E_p, E_0 are the plasmon and exciton energies; Γ_p, Γ_0 are the linewidths of the plasmon and PL; g is the coupling strength; E_{\pm} is the intrinsic energy. α, β are the Hopfield coefficients for the plasmon and exciton contributions, respectively, that satisfy condition $|\alpha|^2 + |\beta|^2 = 1$. They account for the linear combination of the plasmonic and excitonic states. Solving the Eq. (1), we

could obtain the expression for intrinsic energy E_{\pm} as [18]

$$E_{\pm} = \frac{1}{2} \left[E_p + E_0 \pm \sqrt{4g^2 + \left(\delta - \frac{i}{2} (\Gamma_p - \Gamma_0) \right)^2} \right] \quad (2)$$

where $\delta = E_p - E_0$ is the detuning, referring to the energy difference between the plasmon and exciton. The energy peaks above the exciton energy are called the high energy branch (HEB), while those below the exciton energy are called the low energy branch (LEB). The energy difference between the HEB and LEB is named as vacuum Rabi splitting ($\hbar\Omega$), when $E_p = E_0$. We fit the experimental data in the dispersion curves by Eq. (2). Rabi splitting in our experiment is calculated as $\hbar\Omega = \sqrt{4g^2 - \left(\frac{\Gamma_p - \Gamma_0}{2} \right)^2} = 137$ meV. The plasmon linewidth of HNPoM was extracted to be $\Gamma_p = 125$ meV and the exciton linewidth was found to be $\Gamma_0 = 72$ meV (Fig. S4). Thus, it satisfies the stricter strong coupling criterion, $\hbar\Omega \geq (\Gamma_p + \Gamma_0)/2$ [4,9,18]. Moreover, the Hopfield coefficients are calculated to estimate the components of the excitons and plasmons in the strong coupling system. As shown in Fig. 2(f), when $\delta < 0$, the HEB is primarily due to the energy contribution of excitons, while the LEB is mainly attributed to the energy contribution of plasmons. Conversely, when $\delta > 0$, the energy contributions are reversed. Specifically, at zero detuning, the Hopfield coefficients of HEB and LEB are close to 0.5, indicating that the plasmon and exciton states are coupled to form new hybrid states.

For comparison, Ag nanocubes (100 nm in edge length) and Au spheres (160 nm in diameter) instead of Au nanoplates are used to construct the NCoM and NPoM nanocavities and form the typical magnetic modes. Thus, the coupling between MIM and monolayer WSe₂ is studied at room temperature. The experimental results are shown in Fig. S5 and S6. By measuring several NPs of different sizes, scattering spectra with mode splitting are obtained, and the anti-crossing curve is also plotted. After fitting the experimental data, the splitting energy is estimated to be 100 meV and 127 meV respectively for nanocubes and nanospheres, which are less than the splitting used nanoplates. It is worth noting that the magnetic modes of NCoM and NPoM have a larger linewidth than the RBMs of HNPoM. So to more accurately compare these coupled systems, we can use the parameter $2g/(\Gamma_p + \Gamma_0)$. The values are calculated as 0.70, 0.42 and 0.57 for nanoplates, nanocubes, and nanospheres, respectively. Thus, the experimental data indicates the RBM in HNPoM is more suitable for strong coupling investigation. The detailed reasons for the larger coupling strength with RBM than that with nanocubes and nanospheres need to be further studied.

4. Effect of the nanoparticle morphology on strong coupling

NPs with various shapes have been used to form different nanocavities for achieving strong coupling, such as triangles, hexagons, and disks. However, the mechanism of nanoparticle morphology on the coupling is still unclear. Here, within the nanoparticle-on-mirror planar configurations, we investigate the dependence of the modes and the coupling on different morphology. In Figs. 3(a) and (b), we gradually vary a triangle-shaped nanoparticle into a 150 nm hexagonal shape by gradually cutting the angles. From an experimental point of view, synthesized Au nanoplates can easily have both shapes and transitional shapes in between. From the scattering (Fig. 3(a)) and absorption (Fig. 3(b)) spectra, one bright (RBM, red markers) and one dark (quadruple-quadruple mode, blue markers) were observed. Due to the decrease in the particle size, the two modes are overall blue-shifted with different "speeds". However, no matter how the shape changes, these modes can always exist, and no new mode was induced. Likewise, we reshaped the 150 nm hexagonal nanoplate into a nanodisk by changing the rounding of the corners (Figs. 3(c) and (d)). Interestingly, the scattering and absorption spectra do not change with the shape variance and the RBM mode degenerates into well-known l_{01} mode in the end.

Again, this infers that exhausting all possibilities of shapes of the nanoparticle may not strikingly improve the strong coupling.

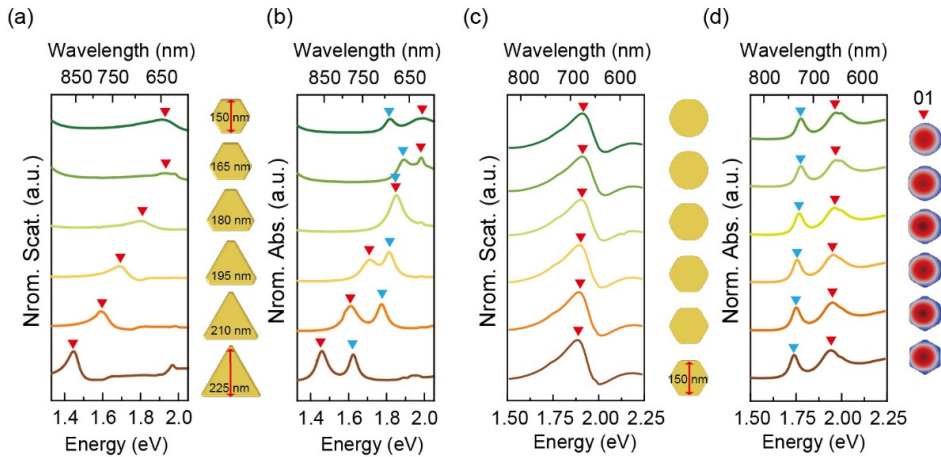


Fig. 3. Nanoparticle-on-mirror planar structures with different morphology. Scattering (a, c) and absorption (b, d) cross-sections of nanocavities consisted with a hexagon changing to a triangle (disk). The gap is set as a 9-nm-thick Al_2O_3 .

To prove that, we explored the influence of morphology on the Rabi splitting. Three kinds of nanoplates are studied: a standard hexagon, a triangle, and a polygon between the triangle and the hexagon. In the simulation, the nanoplate thickness, rounded corner radius, and nanogap thickness (a 9-nm Al_2O_3 on an Ag film) are set to the same. By tuning the nanoplate size, the RBMs of three nanoplates are tuned to 750 nm, matching the exciton energy of monolayer WSe_2 . Figure 4(a) shows the calculated scattering spectra of the three nanoplates coupling with monolayer WSe_2 . All spectra have Rabi splitting features, and the splittings appear to be similar to each other. In general, Rabi splitting is not sensitive to morphological deformation, which means that the influence of particle shape on the coupling can be ignored. To further compare the coupling performance of different NP morphologies with TMDCs, we extract data from a large number of published works [10,12–17,19–22,26,27,41–54] and perform a statistical review, as shown in Fig. 4(b). The detailed data are presented in Table S1. To account for the inclusion of different TMDCs, the material-related parameter of the exciton transition dipole moment, μ , is used as the denominator of the ordinate. It can be observed that the coupling performance does not depend on NP morphology, whether for single NPs or MIM nanocavities. The $2g/\mu$ values are mostly concentrated in the range of 5–20. The overall coupling strength is dropping with the physical dimensions due to the increase of mode volume. It indicates the mode volume (proportional to area and perimeter) plays a more significant role, although larger cavities mean more excitons involved in the coupling process. Furthermore, the statistical results reveal that the gap plasmon mode from MIM nanocavity has a better coupling performance compared with the single NPs due to their more localized electric field. Thus, efforts to achieve a stronger coupling through changes in the nanoparticle morphology can be limited.

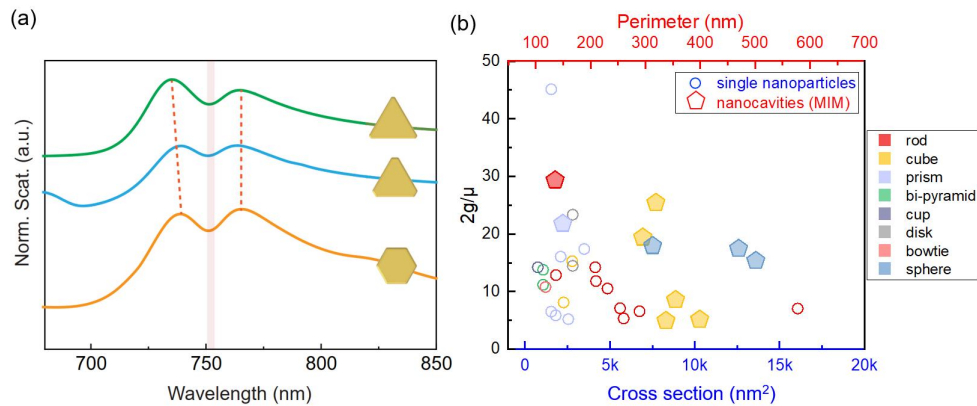


Fig. 4. (a) Rabi splitting in the scattering spectra of three kinds of nanoplates coupled with monolayer WSe_2 . (b) Coupling performance of TMDCs coupled with various plasmonic nanostructures. Color means different morphologies of NPs. For individual NPs, the cross sections of NPs are used as characteristic dimensions, while for the MIM nanocavities, the perimeters of NPs are used.

5. Conclusion

We demonstrated that the strong coupling between Au hexagonal NPs (RBM) and monolayer WSe_2 (excitons) at room temperature leads to approximately 137 meV Rabi splitting. In addition, research has found that changing the morphology of nanoplates does not effectively tune the coupling splitting of the plexcitonic system. This is because, for a metal-insulator-metal nanocavity coupling with monolayer TMDC excitons, the effective coupling region is always near the boundary where the nanocavity has the in-plane vacuum field.

Funding. National Natural Science Foundation of China (12274334, 12204362, 11904271); Natural Science Foundation of Hubei Province (2024AFB769).

Disclosures. The authors declare no conflicts of interest.

Data availability. Data underlying the results presented in this paper are not publicly available at this time but may be obtained from the authors upon reasonable request.

Supplemental document. See [Supplement 1](#) for supporting content.

References

1. J. P. Reithmaier, G. Sek, A. Löffler, *et al.*, "Strong coupling in a single quantum dot-semiconductor microcavity system," *Nature* **432**(7014), 197–200 (2004).
2. D. S. Dovzhenko, S. V. Ryabchuk, Y. P. Rakovich, *et al.*, "Light-matter interaction in the strong coupling regime: Configurations, conditions, and applications," *Nanoscale* **10**(8), 3589–3605 (2018).
3. P. Vasa and C. Lienau, "Strong Light-Matter Interaction in Quantum Emitter/Metal Hybrid Nanostructures," *ACS Photonics* **5**(1), 2–23 (2018).
4. G. Khitrova, H. M. Gibbs, M. Kira, *et al.*, "Vacuum Rabi splitting in semiconductors," *Nat. Phys.* **2**(2), 81–90 (2006).
5. H. Wei, X. Yan, Y. Niu, *et al.*, "Plasmon-exciton interactions: spontaneous emission and strong coupling," *Adv. Funct. Mater.* **31**(51), 2100889 (2021).
6. D. G. Baranov, M. Wersäll, J. Cuadra, *et al.*, "Novel nanostructures and materials for strong light-matter interactions," *ACS Photonics* **5**(1), 24–42 (2018).
7. F. Ge, X. Han, and J. Xu, "Strongly coupled systems for nonlinear optics," *Laser Photonics Rev.* **15**(4), 2000514 (2021).
8. R. F. Ribeiro, J. A. Campos-Gonzalez-Angulo, N. C. Giebink, *et al.*, "Enhanced optical nonlinearities under collective strong light-matter coupling," *Phys. Rev. A* **103**(6), 063111 (2021).
9. G. Zengin, M. Wersäll, S. Nilsson, *et al.*, "Realizing strong light-matter interactions between single-nanoparticle plasmons and molecular excitons at ambient conditions," *Phys. Rev. Lett.* **114**(15), 157401 (2015).
10. M. Geisler, X. Cui, J. Wang, *et al.*, "Single-crystalline gold nanodisks on WS_2 mono- and multilayers for strong coupling at room temperature," *ACS Photonics* **6**(4), 994–1001 (2019).

11. X. Han, K. Wang, Y. Jiang, *et al.*, “Controllable plexcitonic coupling in a WS₂-Ag nanocavity with solvents,” *ACS Appl. Mater. Interfaces* **13**(36), 43554–43561 (2021).
12. M. E. Kleemann, R. Chikkaraddy, E. M. Alexeev, *et al.*, “Strong-coupling of WSe₂ in ultra-compact plasmonic nanocavities at room temperature,” *Nat. Commun.* **8**(1), 1296 (2017).
13. X. Han, K. Wang, X. Xing, *et al.*, “Rabi splitting in a plasmonic nanocavity coupled to a WS₂ monolayer at room temperature,” *ACS Photonics* **5**(10), 3970–3976 (2018).
14. X. Liu, J. Yi, S. Yang, *et al.*, “Nonlinear valley phonon scattering under the strong coupling regime,” *Nat. Mater.* **20**(9), 1210–1215 (2021).
15. J. Wen, H. Wang, W. Wang, *et al.*, “Room-temperature strong light–matter interaction with active control in single plasmonic nanorod coupled with two-dimensional atomic crystals,” *Nano Lett.* **17**(8), 4689–4697 (2017).
16. S. Wang, Q. Le-Van, F. Vaianella, *et al.*, “Limits to strong coupling of excitons in multilayer WS₂ with collective plasmonic resonances,” *ACS Photonics* **6**(2), 286–293 (2019).
17. J. Cuadra, D. G. Baranov, M. Wersall, *et al.*, “Observation of tunable charged exciton polaritons in hybrid monolayer WS₂-plasmonic nanoantenna system,” *Nano Lett.* **18**(3), 1777–1785 (2018).
18. M. Pelton, S. D. Storm, and H. Leng, “Strong coupling of emitters to single plasmonic nanoparticles: Exciton-induced transparency and Rabi splitting,” *Nanoscale* **11**(31), 14540–14552 (2019).
19. D. Zheng, S. Zhang, Q. Deng, *et al.*, “Manipulating coherent plasmon–exciton interaction in a single silver nanorod on monolayer WSe₂,” *Nano Lett.* **17**(6), 3809–3814 (2017).
20. M. Stuhrenberg, B. Munkhbat, D. G. Baranov, *et al.*, “Strong light-matter coupling between plasmons in individual gold bi-pyramids and excitons in mono- and multilayer WSe₂,” *Nano Lett.* **18**(9), 5938–5945 (2018).
21. C. Li, X. Lu, A. Srivastava, *et al.*, “Second harmonic generation from a single plasmonic nanorod strongly coupled to a WSe₂ monolayer,” *Nano Lett.* **21**(4), 1599–1605 (2021).
22. T. Zhang, Q. Guo, Z. Shi, *et al.*, “Coherent second harmonic generation enhanced by coherent plasmon–exciton coupling in plasmonic nanocavities,” *ACS Photonics* **10**(5), 1529–1537 (2023).
23. P. Jiang, G. Song, Y. Wang, *et al.*, “Tunable strong exciton-plasmon-exciton coupling in WS₂-J-aggregates-plasmonic nanocavity,” *Opt. Express* **27**(12), 16613–16623 (2019).
24. X. Zong, L. Li, K. Yu, *et al.*, “Enhanced light–matter interactions in ultrathin transition-metal-dichalcogenide metasurfaces by magnetic and toroidal dipole bound states in the continuum,” *Opt. Express* **30**(24), 43104–43117 (2022).
25. R. Chikkaraddy, B. De Nijs, F. Benz, *et al.*, “Single-molecule strong coupling at room temperature in plasmonic nanocavities,” *Nature* **535**(7610), 127–130 (2016).
26. J. Qin, Y.-H. Chen, Z. Zhang, *et al.*, “Revealing strong plasmon-exciton coupling between nanogap resonators and two-dimensional semiconductors at ambient conditions,” *Phys. Rev. Lett.* **124**(6), 063902 (2020).
27. L. Yang, X. Xie, J. Yang, *et al.*, “Strong light-matter interactions between gap plasmons and two-dimensional excitons under ambient conditions in a deterministic way,” *Nano Lett.* **22**(6), 2177–2186 (2022).
28. J. Y. Li, W. Li, J. Liu, *et al.*, “Room-temperature strong coupling between a single quantum dot and a single plasmonic nanoparticle,” *Nano Lett.* **22**(12), 4686–4693 (2022).
29. L. Liu, L. Y. M. Tobing, T. Wu, *et al.*, “Plasmon-induced thermal tuning of few-exciton strong coupling in 2D atomic crystals,” *Optica* **8**(11), 1416–1423 (2021).
30. A. Amo, T. Liew, C. Adrados, *et al.*, “Exciton–polariton spin switches,” *Nat. Photonics* **4**(6), 361–366 (2010).
31. A. Wallraff, D. I. Schuster, A. Blais, *et al.*, “Strong coupling of a single photon to a superconducting qubit using circuit quantum electrodynamics,” *Nature* **431**(7005), 162–167 (2004).
32. J. McKeever, A. Boca, A. D. Boozer, *et al.*, “Experimental realization of a one-atom laser in the regime of strong coupling,” *Nature* **425**(6955), 268–271 (2003).
33. C. Schneider, A. Rahimi-Iman, N. Y. Kim, *et al.*, “An electrically pumped polariton laser,” *Nature* **497**(7449), 348–352 (2013).
34. V. Ardizzone, F. Riminucci, S. Zanotti, *et al.*, “Polariton Bose–Einstein condensate from a bound state in the continuum,” *Nature* **605**(7910), 447–452 (2022).
35. J. Simon, H. Tanji, J. K. Thompson, *et al.*, “Interfacing collective atomic excitations and single photons,” *Phys. Rev. Lett.* **98**(18), 183601 (2007).
36. G. Wendin, “Quantum information processing with superconducting circuits: a review,” *Rep. Prog. Phys.* **80**(10), 106001 (2017).
37. S. Balci and C. Kocabas, “Ultra hybrid plasmonics: Strong coupling of plexcitons with plasmon polaritons,” *Opt. Lett.* **40**(14), 3424 (2015).
38. F.-P. Schmidt, H. Ditlbacher, U. Hohenester, *et al.*, “Dark plasmonic breathing modes in silver nanodisks,” *Nano Lett.* **12**(11), 5780–5783 (2012).
39. M. K. Krug, M. Reisecker, A. Hohenau, *et al.*, “Probing plasmonic breathing modes optically,” *Appl. Phys. Lett.* **105**(17), 171103 (2014).
40. A. Campos, A. Arbouet, J. Martin, *et al.*, “Plasmonic breathing and edge modes in aluminum nanotriangles,” *ACS Photonics* **4**(5), 1257–1263 (2017).
41. R. Ai, X. Xia, H. Zhang, *et al.*, “Orientation-dependent interaction between the magnetic plasmons in gold nanocups and the excitons in WS₂ monolayer and multilayer,” *ACS Nano* **17**(3), 2356–2367 (2023).

42. R. Du, H. Hu, T. Fu, *et al.*, “How to obtain the correct rabi splitting in a subwavelength interacting system,” *Nano Lett.* **23**(2), 444–450 (2023).
43. S. Hou, L. Y. M. Tobing, X. Wang, *et al.*, “Manipulating coherent light–matter interaction: Continuous transition between strong coupling and weak coupling in MoS₂ monolayer coupled with plasmonic nanocavities,” *Adv. Opt. Mater.* **7**(22), 1900857 (2019).
44. A. Hu, W. Zhang, W. Liu, *et al.*, “Local plasmon phase delay effect in plasmon–exciton coupling,” *Adv. Opt. Mater.* **10**(9), 2102380 (2022).
45. Y. Jiang, H. Wang, S. Wen, *et al.*, “Resonance coupling in an individual gold nanorod–monolayer WS₂ heterostructure: Photoluminescence enhancement with spectral broadening,” *ACS Nano* **14**(10), 13841–13851 (2020).
46. C. Li, H. Luo, L. Hou, *et al.*, “Giant photoluminescence enhancement of monolayer WSe₂ using a plasmonic nanocavity with on-demand resonance,” *Nano Lett.* **24**(19), 5879–5885 (2024).
47. B. Munkhbat, D. G. Baranov, A. Bisht, *et al.*, “Electrical control of hybrid monolayer tungsten disulfide–plasmonic nanoantenna light–matter states at cryogenic and room temperatures,” *ACS Nano* **14**(1), 1196–1206 (2020).
48. J. Sun, H. Hu, D. Zheng, *et al.*, “Light-emitting plexciton: Exploiting plasmon–exciton interaction in the intermediate coupling regime,” *ACS Nano* **12**(10), 10393–10402 (2018).
49. Y. Wang, Q. You, Z. Li, *et al.*, “Strong coupling of plasmonic nanorods with a MoSe₂ monolayer in the near-infrared shortwave region,” *J. Phys. Chem. C* **128**(12), 5280–5287 (2024).
50. M. Wang, A. Krasnok, T. Zhang, *et al.*, “Tunable fano resonance and plasmon–exciton coupling in single Au nanotriangles on monolayer WS₂ at room temperature,” *Adv. Mater.* **30**(22), 1705779 (2018).
51. J. Wen, H. Wang, H. Chen, *et al.*, “Room-temperature strong coupling between dipolar plasmon resonance in single gold nanorod and two-dimensional excitons in monolayer WSe₂,” *Chin. Phys. B* **27**(9), 096101 (2018).
52. P. Xie, Z. Liang, Z. Li, *et al.*, “Coherent and incoherent coupling dynamics in a two-dimensional atomic crystal embedded in a plasmon-induced magnetic resonator,” *Phys. Rev. B* **101**(4), 045403 (2020).
53. A. B. Yankovich, B. Munkhbat, D. G. Baranov, *et al.*, “Visualizing spatial variations of plasmon–exciton polaritons at the nanoscale using electron microscopy,” *Nano Lett.* **19**(11), 8171–8181 (2019).
54. J. Zhong, J.-Y. Li, J. Liu, *et al.*, “Room-temperature strong coupling of few-exciton in a monolayer WS₂ with plasmon and dispersion deviation,” *Nano Lett.* **24**(5), 1579–1586 (2024).